

Radial pulsation as a function of hydrogen abundance

C. S. Jeffery^{*} & H. Saio[†]

Armagh Observatory, College Hill, Armagh BT61 9DG, Northern Ireland

Astronomical Institute, School of Science, Tohoku University, Sendai 980-8578, Japan

Accepted Received 2016 April 1; in original form 2016 April 1

ABSTRACT

Using linear non-adiabatic pulsation analysis, we explore the radial-mode (p-mode) stability of stars across a wide range of mass ($0.2 \leq M \leq 50 M_{\odot}$), composition ($0 \leq X \leq 0.7$, $Z = 0.001, 0.02$), effective temperature ($3000 \leq T_{\text{eff}} \leq 40\,000$ K), and luminosity ($0.01 \leq L/M \leq 100,000$ solar units). We identify the instability boundaries associated with low- to high-order radial oscillations ($0 \leq n \leq 16$). The instability boundaries are a strong function of both composition and radial order (n). With decreasing hydrogen abundance we find that i) the classical blue edge of the Cepheid instability strip shifts to higher effective temperature and luminosity, and ii) high-order modes are more easily excited and small islands of high radial-order instability develop, some of which correspond with real stars. Driving in all cases is by the classical κ -mechanism and/or strange modes. We identify regions of parameter space where new classes of pulsating variable may, in future, be discovered. The majority of these are associated with reduced hydrogen abundance in the envelope; one has not been identified previously.

Key words: stars: oscillations, stars: interiors, stars: chemically peculiar, stars: variables: general

1 INTRODUCTION

Since the discovery of periodic light variations in the luminous giant δ Cephei, the study of stellar pulsations has transformed our understanding of how stars work, as well as establishing a distance scale whereby the cosmos can be measured. The fact that the light variations in δ Cep represented a major discovery testifies to the fact that not all stars are variable. However, as telescopes and detectors have become more sensitive, pulsations have been identified in diverse groups of stars of all masses and across the Hertzsprung-Russell diagram. Such discoveries continue to the present day, with pulsations in low-mass white dwarfs and pre-white dwarfs being the latest additions to the pulsating star zoo (Fig. 1) (Maxted et al. 2013; Hermes et al. 2013).

Jeffery & Saio (2013) demonstrated that pulsation instability in the low-mass pre-white dwarf J0247-25B would arise in a high-order overtone if the envelope was depleted in hydrogen. The principal reason for this, demonstrated previously by Saio & Jeffery (1988) and Jeffery & Saio (2007), is that hydrogen acts as a poison, suppressing the positive opacity gradient around an opacity peak which would otherwise drive pulsations if located at an appropriate depth beneath the stellar surface¹.

The question therefore arose whether it would be possible to predict the properties of other hitherto undiscovered pulsating variables, especially those in which hydrogen has been depleted as a consequence of prior evolution. Consequently, we have carried out a parametric survey in order to identify locations where new classes of variable star await discovery.

2 RADIAL PULSATION MODELS

The investigation commenced by computing a grid of 258,000 models of stellar envelopes covering a range of chemical mixtures and for masses on the range $0.2 \leq M/M_{\odot} \leq 50$, effective temperatures $\log T_{\text{eff}}/\text{K} = 3.50(0.02)4.60$, and luminosity-to-mass ratios $\log(L/L_{\odot})/(M/M_{\odot}) = -2.0(0.2)5.0$. The linear nonadiabatic analysis of stability

¹ The condition for driving an oscillation by the κ -mechanism in such a region is generally understood to be that the spatial derivative $d(\kappa_T + \kappa_{\rho}/(\Gamma_3 - 1))/dr > 0$, where κ_T and κ_{ρ} are the temperature and density derivatives of the opacity κ , and Γ_3 is the usual adiabatic exponent (Unno et al. 1989, p. 243).

* E-mail: csj@arm.ac.uk

† E-mail: saio@astr.tohoku.ac.jp

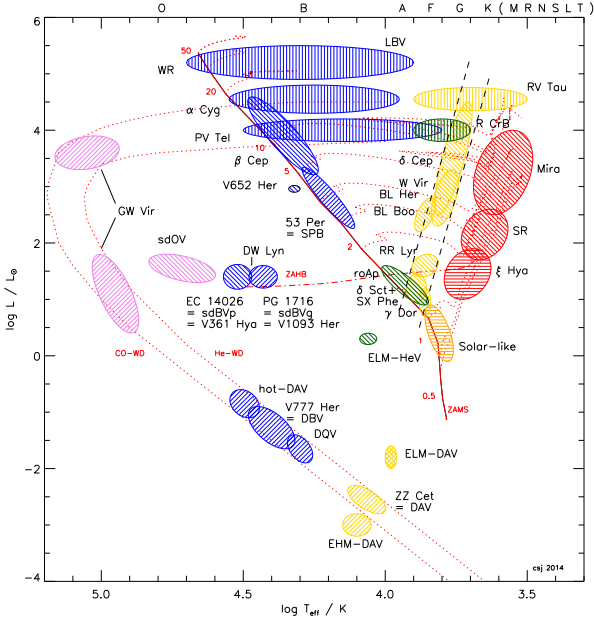


Figure 1. Luminosity-effective temperature (or Hertzsprung-Russell) diagram showing the approximate locations of major pulsating variables coloured roughly by spectral type, the zero-age main sequence and horizontal branch, the Cepheid instability strip, and evolution tracks for model stars of various masses, indicated by small numbers (M_{\odot}). Shadings represent opacity-driven p-modes (\\), g-modes (///) and strange modes (|||) and acoustically-driven modes (≡). Approximate spectral types are indicated on the top axis. Based on figures by J. Christensen-Dalsgaard and subsequently by Jeffery (2008a).

against pulsation was carried out following methods described by Saio et al. (1983) and Jeffery & Saio (2006a,b).

The OPAL95 (Iglesias & Rogers 1996) opacities were adopted, except at low temperatures, where Alexander & Ferguson (1994) opacities were used. As a test of sensitivity to opacity, additional calculations were made with OP opacities (Badnell et al. 2005). Convection is treated assuming a standard mixing-length theory with the ratio mixing-length to pressure scale height $l/H_p = 1.5$. Any convection/pulsation interaction is neglected by setting the divergence of the convective flux perturbation to zero. Therefore results for $T_{\text{eff}} < 4000$ K should be treated with caution.

The outer boundary for the envelope model is set at the Rosseland mean optical depth $\tau = 10^{-3}$. The integration is carried out with pressure $\log_{10} P$ as the independent variable, with initial stepsize $\delta \log_{10} P = 0.02$, which is adjusted to maintain increments in radius $\delta r/r < 0.01$, density $\delta \rho/\rho < 0.1$ and electron pressure $\delta P_e/P_e < 0.08$ at each step. The integration is halted at a fractional mass $m = M_{\star}/10$ or fractional radius $r = R_{\star}/100$, whichever occurs first.

For each model envelope, the first 17 eigenfrequencies were located and stored, including the real and imaginary components ω_r and ω_i , the period Π and the number of nodes in the eigensolution. Modes with $\omega_i < 0$ were deemed to be unstable, *i.e.* pulsations could be excited.

We considered a range of abundances with hydrogen-mass fraction $X = 0.002, 0.1, 0.30$ and 0.70 and metal mass fraction $Z = 0.001$ and 0.02 . We have assumed that the iron

and nickel abundances are scaled to solar values (metal mixture GN93: Grevesse & Noels 1993) for all values of Z . We have *not* considered any additional enhancements to iron-group or other elements.

The results are presented primarily as contour plots representing the number of unstable modes as a function of $(T_{\text{eff}}, L/M)$ for each composition (Figs. 2 and A.1 – A.8). This provides an overall instability boundary since it includes pulsations in both low- and high-order modes. In some cases, envelope models with very high L/M ratios and/or very low T_{eff} were difficult to integrate due to very low densities in the equation of state; these appear as voids on the contour plots.

Second, the instability boundaries for modes with $n = 0, 1$, or more nodes, *i.e.* the instability boundaries for the fundamental radial, and for the first and higher overtone pulsations are shown, also as a function of $(T_{\text{eff}}, L/M)$ (Figs. 3 and A.9 – A.16).

It is noted that many models may not represent any known stars (*e.g.* high M models with very low L/M .) Nevertheless, exploring such models provides a systematic insight into the pulsation properties of stars in general.

3 RADIAL-MODE INSTABILITY

The use of L/M to parameterize the model grid exploits the fact that the radial pulsation properties of stellar envelopes are only slowly dependent on the mass of the star over a range from 0.2 to $50 M_{\odot}$ (cf. Fig. 2: top row). Nevertheless there are significant features to note; details may be verified from figures in Appendix A.

At $X = 0.70, Z = 0.02$ (Figs. A.1 and A.9):

- i) The most familiar feature is the classical Cepheid instability strip running diagonally toward high L/M and low T_{eff} at $\log L/M > 0$. The principal driving is provided by the second ionization of singly-ionized helium (He^+).
- ii) This is supplemented by an adjacent and parallel strip at lower T_{eff} in which higher-order modes are excited (cf. Fig. 3: top row). This may be related to the solar-like oscillations detected by *Corot* and *Kepler* in many less luminous red giants (Miglio et al. 2009; Bedding et al. 2010; Huber et al. 2010) and marked as ξ Hya variables in Fig. 1. Although the latter are generally thought to be excited stochastically by turbulence, the *order* of the p-modes detected in red giants decreases as the luminosity increases, which is consistent with our prediction from the kappa-mechanism. Xiong & Deng (2007) report from a non-adiabatic analysis including coupling between convection and pulsations that these modes are excited. We hence find that evidence exists for a contribution of the kappa-mechanism from ionization of H and He^0 to the driving of small-amplitude oscillations in red giants.
- iii) The low T_{eff} strip extends to very low L/M values and is responsible in low-mass main-sequence stars for δ Scuti variables. The principal driving comes from H and He^0 ionisation, although the high overtone pulsations in hotter δ Sct stars are probably associated with He^+ ionization (*i.e.* the classical instability strip), which extends to the main sequence with $\log g < \sim 5, \log L/M > \sim 0$.
- iv) At high L/M , models show instability in one or

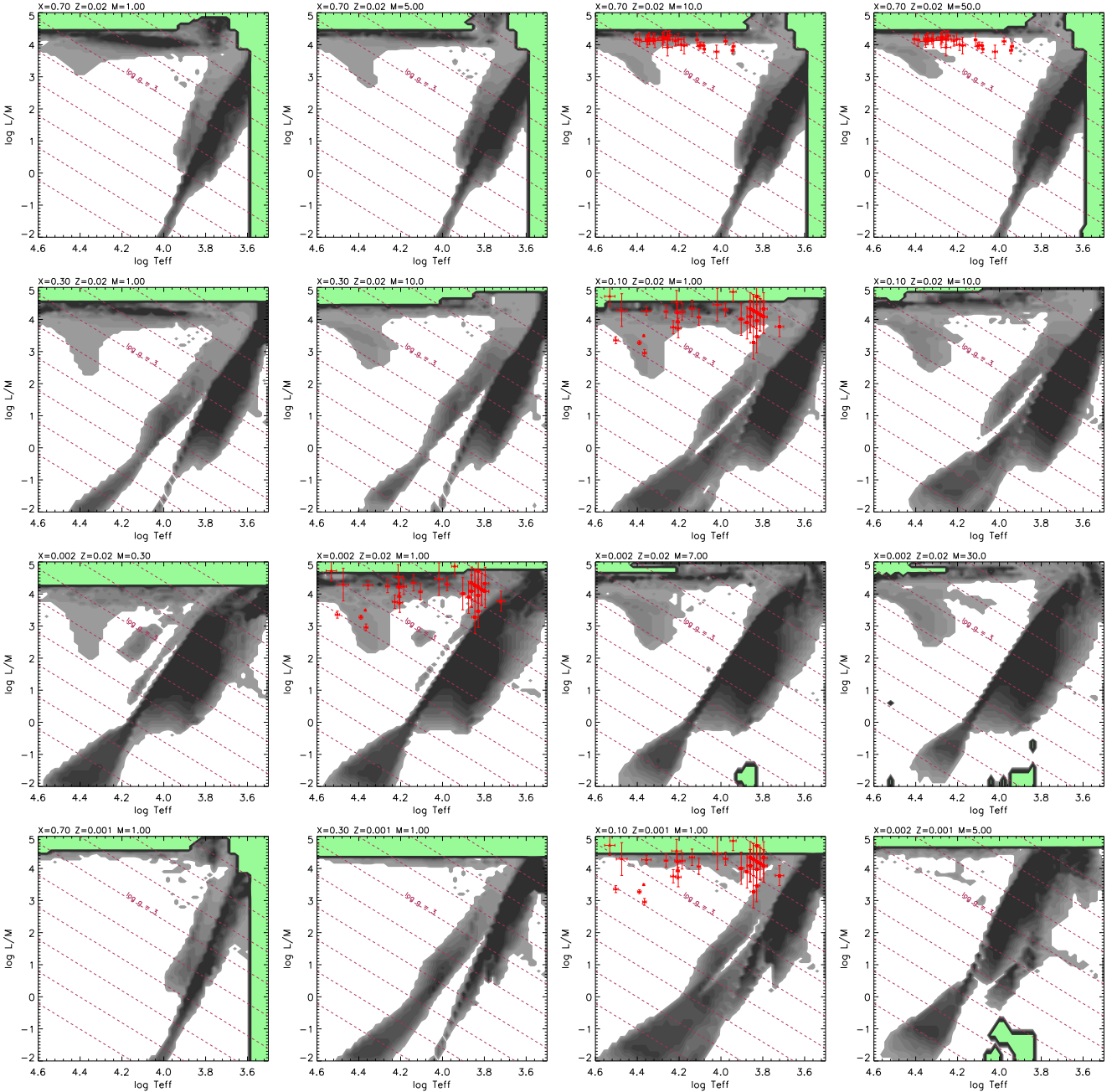


Figure 2. Unstable pulsation modes in stars with homogeneous envelopes for selected compositions and masses, as labelled. Full grids are shown in Appendix A. The *number* of unstable radial modes is represented by grey scale contours, with the lightest shade marking the instability boundary (one unstable mode), and the darkest shade representing ten or more unstable modes. Broken (maroon online) diagonal lines represent contours of constant surface gravity at $\log g = 8, 7, 6, \dots, 1$. Pale green areas denote regions where envelope models encountered convergence difficulties. Red symbols with error bars shown on selected panels represent the observed positions of pulsating low-mass hydrogen-deficient stars, including extreme helium stars and R Coronae Borealis variables (Jeffery 2008b), shown on panels with $X \leq 0.1$ and $M = 1.0 M_{\odot}$, and α Cyg variables (Crowther et al. 2006; Searle et al. 2008; Farnstein & Przybilla 2012), shown on panels with $X = 0.7, Z = 0.02$ and $M \geq 10 M_{\odot}$. Figs. 2 and 3 are best viewed online and expanded; one grid is enlarged in Fig. 4.

more modes; these are the so-called *strange* modes (Gautschy & Glatzel 1990; Saio et al. 1998). The general confusion in the mode boundary diagram (Fig. A.9) is accounted for by a breakdown in the strict 1-1 correspondence between mode eigenfrequency and node number for strange

modes² α Cygni variables can be explained by strange

² Strange modes in high L/M stars are essentially as defined by Gautschy & Glatzel (1990); Saio et al. (1998), and first identified by Wood (1976). Other modes of somewhat different character have also been described as *strange*, e.g. by Buchler et al. (1997);

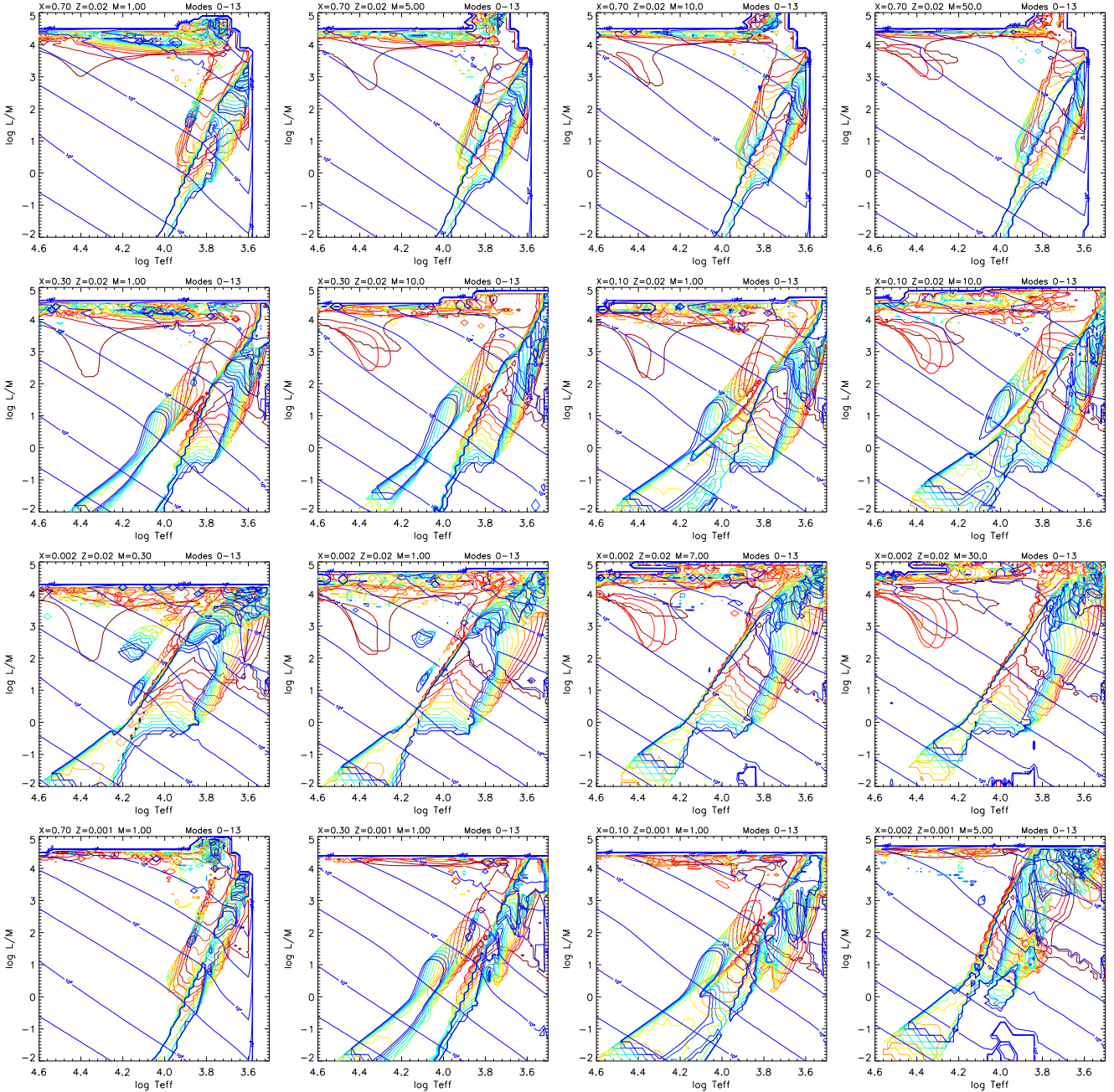


Figure 3. As Fig. 2, but showing the *boundaries* for individual radial modes as coloured contours, with the darkest red representing the boundary of the fundamental ($n = 0$) mode, with increasing higher orders ($n = 1 - 10$) represented progressively by colours of increasing frequency (orange, yellow, green, blue ...). Solid blue lines represent contours of equal fundamental radial-mode period in seconds spaced at decadal intervals.

modes, if considerable mass has been lost (Saio et al. 2013).

v) At $\log L/M > 3$ and $\log T_{\text{eff}} \approx 4.4$ there is a weak instability finger caused by iron-group opacities at temperatures $T \approx 2 \times 10^5$ K. This can be identified with β Cepheid variables on the upper main sequence. The shape of this finger is sensitive to mass, and also to the iron and nickel

Buchler & Kolláth (2001); Smolec (2016). The current analysis makes no distinction between *strange* and *normal* modes; it only identifies which modes are stable or unstable.

abundances (Jeffery & Saio 2007).

At $X = 0.30, Z = 0.02$ (Figs. A.2 and A.10), a modest reduction in hydrogen abundance has the effect of increasing the driving effect of helium in the classical instability strip and iron in the ‘Z-bump’ instability finger. The chief consequences are:

i) As the mean molecular weight in the envelope increases, the He^+ instability strip shifts to higher T_{eff} . With the excitation of higher-order radial modes, the strip also

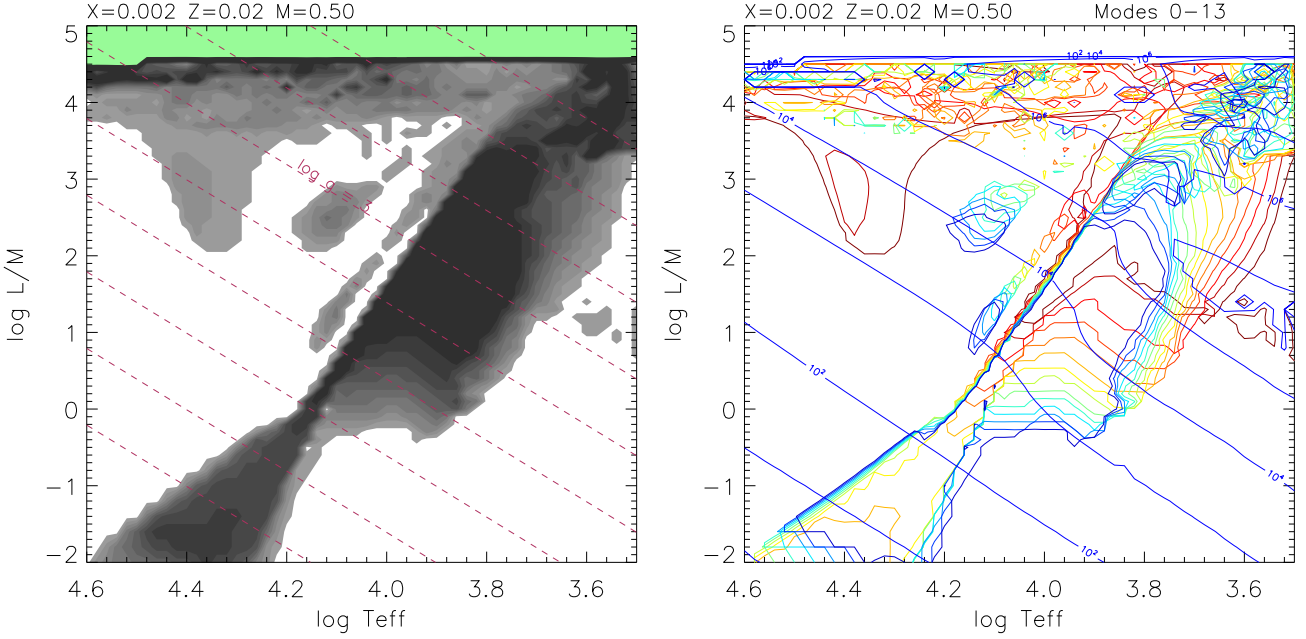


Figure 4. As Figs. 2 and 3, for composition $X = 0.002$, $Z = 0.02$, $M = 0.50 M_{\odot}$, enlarged for clarity.

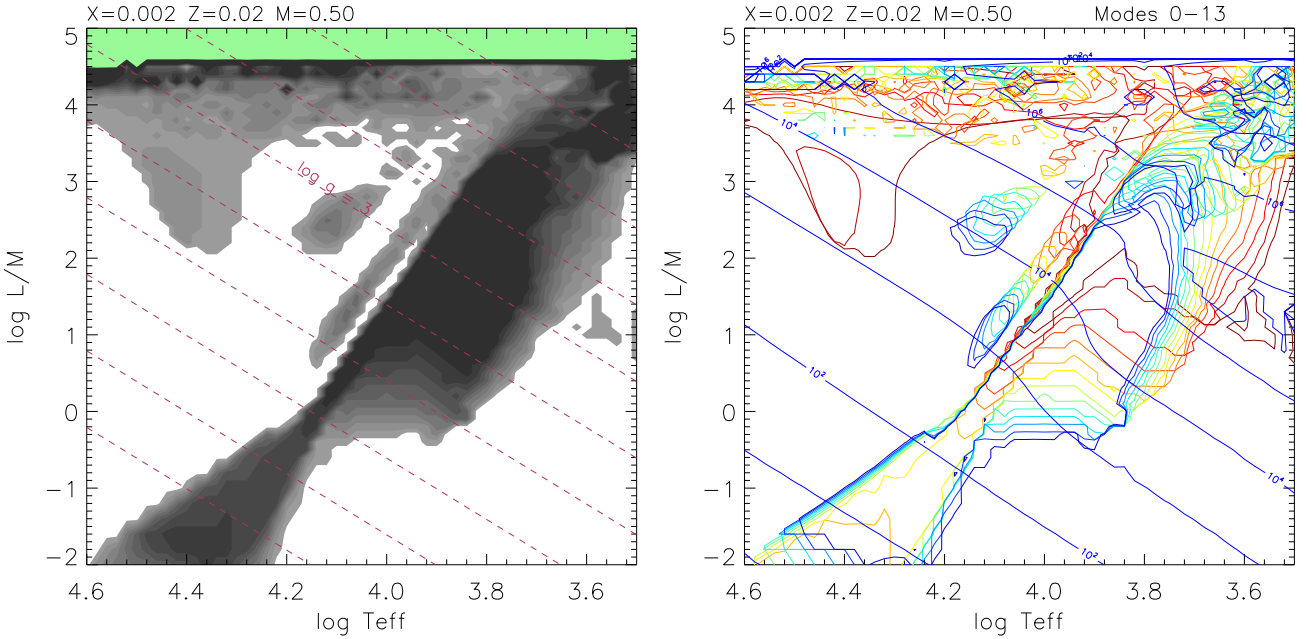


Figure 5. As Fig. 4 with OP opacities rather than OPAL95 opacities.

extends to lower L/M .

ii) For $\log L/M < -1$ the high-order strip narrows significantly.

iii) With increasing contrast between iron-group and hydrogen opacity, the ‘Z-bump’ finger becomes significantly stronger.

iv) At high mass, ‘Z-bump’ excited fundamental modes extend to $\log T_{\text{eff}} \approx 4.0$, forming a ‘spur’ to the ‘Z-bump’ finger. Close inspection of these modes show an unrealisti-

cally large amplitude propagating deep into the interior (to fractional mass $m/M < 0.001$); we do not consider these to be real.

At $X = 0.10$, $Z = 0.02$ (Figs. A.3 and A.11), the consequences of reducing the hydrogen abundance seen at $X = 0.3$ continue. In addition:

i) The width of the high-order He^+ instability strip at low L/M increases. As mass increases, the region becomes

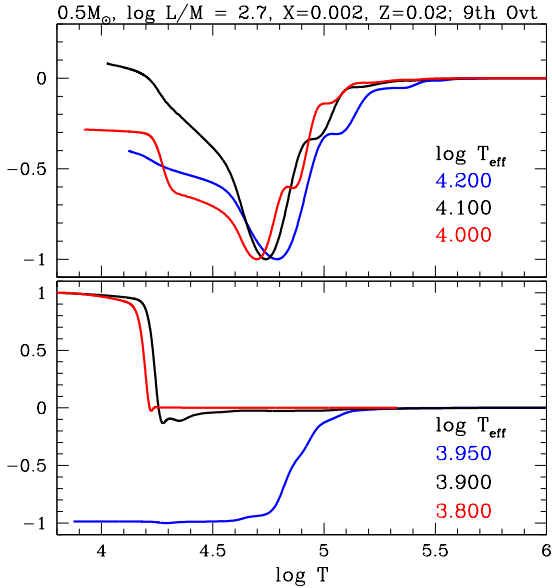


Figure 6. Work integrals W as a function of temperature for the 9th overtone in the neighbourhood of the instability island at $X = 0.002$, $Z = 0.02$, with $M = 0.5 M_{\odot}$, $\log L/M = 2.7$, and $\log T_{\text{eff}}$ as shown. Positive values of W at the surface indicate instability. At $\log T_{\text{eff}} \leq 3.9$, driving is due to He^0 ionization – essentially the classical Cepheid mechanism. For $\log T_{\text{eff}} = 3.95$, 4.0 and 4.2, the mode is stable. For $\log T_{\text{eff}} = 4.1$, the mode is unstable due to driving by both He^0 and He^+ ionization.

fragmented.

- ii) For $\log L/M < -1$, there are virtually no unstable modes in the high-order strip.
- iii) The Z-bump finger extends to $\log L/M > 2.0$; the high-mass spur persists, but see above.

At $X = 0.002$, $Z = 0.02$ (Figs. A.4 and A.12), the consequences of reducing the hydrogen abundance seen at $X = 0.1$ continue. In addition:

- i) At $M < 5 M_{\odot}$, an additional narrow strip of high-overtone instability is seen immediately to the blue of the He^+ instability strip at $\log L/M \approx 1$. This strip has been identified with pulsations observed in J0247-25B (Jeffery & Saio 2013).
- ii) The Z-bump finger is very strong and broad, but only low-order ($n < 4$) modes are excited; the high mass $n = 0$ Z-bump spur persists.
- iii) The width of the high-order He^+ instability strip at low L/M remains large. At low mass, the models give evidence that radial modes in some DB white dwarfs may be unstable, as previously shown by Kawaler (1993).
- iv) At $M < 2 M_{\odot}$, an island of high-overtone instability is seen around $\log T_{\text{eff}} \approx 4.1$ and $\log L/M \approx 2 - 3$ (Fig. 4), diminishing in extent with increasing mass. This island has appeared in previous calculations (Jeffery & Saio 2013), but only here identified as a persistent feature over a range of masses. Driving is due to a combination of He^0 and He^+ ionization (Fig. 6). Since pulsation instability boundaries are sensitive to details of the precise chemical mixture and to the overall opacity calculation, a few of these models were recalculated using OP opacities (Badnell et al. 2005)

instead of OPAL95 opacities (Iglesias & Rogers 1996). Minor differences may be seen (Fig. 5), but the new instability island persists and the differences are small compared with the large variations in X which are of primary interest. We suggest that stars having these characteristics, should they actually occur in nature, would be good candidates to show high-order radial (or non-radial) p -mode pulsations.

At $X = 0.70$, $Z = 0.001$ (Figs. A.5 and A.13), the principal consequence of reducing the metallicity is that the Z-bump finger disappears. In addition, the classical instability strip, and the high-overtone strip to the red are both narrowed.

At $X = 0.002$, $Z = 0.001$ (Figs. A.8 and A.16), the high-overtone instability island identified at $X = 0.002$, $Z = 0.02$ persists but, as there were substantial difficulties computing envelope models with $M < 2 M_{\odot}$ at this composition for other ranges of L/M and T_{eff} , these models are not shown.

At $X = 0.70$, $Z = 0.02$ and $\log L/M \leq 0$ (Fig. A.1), unstable radial modes initially form a single narrow strip, extending the classical Cepheid instability strip to very low L/M . With $X = 0.30$ (Fig. A.2), a second strip develops substantially to the blue of the first. Again, this is the low L/M extension of the He^+ -driven strip already seen. We note that the excited modes are dominated by high-order modes (Fig. A.10). At $X = 0.10$ both strips broaden to form a single region with a complicated mode structure (Figs. A.3, A.11). Finally, at $X = 0.002$, the redward strip stabilizes, to leave only a broad blue instability strip (Fig. A.12). Similar behaviour is replicated at $Z = 0.001$. Predictions of radial instability in both DA and DB white dwarfs are well established (Saio et al. 1983; Kawaler 1993). However there has so far been no successful detection of p -mode pulsations in any white dwarfs (Silvotti et al. 2011; Kilkenny et al. 2014).

4 CONCLUSION

We have made an extensive survey of the stability against radial pulsations for the envelopes of stars having masses in the range $0.2 - 50 M_{\odot}$ and hydrogen abundances (by mass fraction) from $X = 0.70$ to 0.002 , considering both metal-rich ($Z = 0.02$) and metal-poor ($Z = 0.001$) mixtures. The grid of models ranges in effective temperature from $T_{\text{eff}} = 3000 - 40000$ K, and in luminosity-to-mass ratio from $L/M = 0.01 - 100,000$ (in solar units), covering most of parameter space occupied by stars, excepting only the hottest and coolest supergiants, the hottest subdwarfs, the most massive white dwarfs and the coolest supergiants and dwarfs. By considering overtones up to $n = 16$, we identify nearly all stars likely to be unstable to p -mode oscillations driven by the κ -mechanism.

We demonstrate that the Hertzsprung-Russell diagram for pulsation instability expressed as a plot of L/M versus T_{eff} is only slowly variant with mass M , but is much more sensitive to composition, especially the hydrogen abundance since the latter normally acts to damp pulsations.

Within a single computational framework, we recover all hitherto known regions of radial and non-radial p -mode instability due to the κ -mechanism and/or strange modes. The detailed boundaries are likely to vary for specific cases

owing to other properties such as internal composition gradients and long-term evolution effects.

We identify one new region of pulsation instability for low-mass hydrogen-deficient stars with $\log L/M \approx 2-3$ and $\log T_{\text{eff}} \approx 4.0-4.2$; κ -mechanism driving is by He^0 and He^+ ionization. No stars are currently known to exhibit these pulsations.

In addition, we conclude that solar-like oscillations in red giants may be at least partially driven by the κ -mechanism, supporting Xiong & Deng (2007). To investigate this and other questions, a more detailed study of the relative rôles of convection and the κ -mechanism in exciting pulsations across the H-R diagram will follow.

ACKNOWLEDGMENTS

The Armagh Observatory is funded by direct grant from the Northern Ireland Department of Culture, Arts and Leisure.

REFERENCES

- Alexander D. R., Ferguson J. W., 1994, *ApJ*, **437**, 879
 Badnell N. R., Bautista M. A., Butler K., Delahaye F., Mendoza C., Palmeri P., Zeppen C. J., Seaton M. J., 2005, *MNRAS*, **360**, 458
 Bedding T. R., Huber D., Stello D., et al. 2010, *ApJ*, 713, L176
 Buchler J. R., Kolláth Z., 2001, *ApJ*, **555**, 961
 Buchler J. R., Yecko P. A., Kollath Z., 1997, *â*, **326**, 669
 Crowther P. A., Lennon D. J., Walborn N. R., 2006, *A&A*, 446, 279
 Firnstein M., Przybilla N., 2012, *A&A*, 543, A80
 Gautschy A., Glatzel W., 1990, *MNRAS*, **245**, 597
 Grevesse N., Noels A., 1993, in Prantzos N., Vangioni-Flam E., Casse M., eds, *Origin and Evolution of the Elements*. pp 15–25
 Hermes J. J., Montgomery M. H., Winget D. E., Brown W. R., Gianninas A., Kilic M., Kenyon S. J., Bell K. J., 2013, *ApJ*, **765**, 102
 Huber D., Bedding T. R., Stello D., et al. 2010, *ApJ*, **723**, 1607
 Iglesias C. A., Rogers F. J., 1996, *ApJ*, **464**, 943
 Jeffery C. S., 2008a, *Communications in Asteroseismology*, **157**, 240
 Jeffery C. S., 2008b, *Information Bulletin on Variable Stars*, **5817**, 1
 Jeffery C. S., Saio H., 2006a, *MNRAS*, **371**, 659
 Jeffery C. S., Saio H., 2006b, *MNRAS*, **372**, L48
 Jeffery C. S., Saio H., 2007, *MNRAS*, **378**, 379
 Jeffery C. S., Saio H., 2013, *MNRAS*, **435**, 885
 Kawaler S. D., 1993, *ApJ*, 404, 294
 Kilkenny D., Welsh B. Y., Koen C., Gulbis A. A. S., Kotze M. M., 2014, *MNRAS*, 437, 1836
 Maxted P. F. L., et al., 2013, *Nature*, 498, 463
 Miglio A., et al., 2009, *A&A*, 503, L21
 Saio H., Jeffery C. S., 1988, *ApJ*, **328**, 714
 Saio H., Winget D. E., Robinson E. L., 1983, *ApJ*, **265**, 982
 Saio H., Baker N. H., Gautschy A., 1998, *MNRAS*, 294, 622
 Saio H., Georgy C., Meynet G., 2013, *MNRAS*, 433, 1246
 Searle S. C., Prinja R. K., Massa D., Ryans R., 2008, *A&A*, 481, 777
 Silvotti R., Fontaine G., Pavlov M., Marsh T. R., Dhillon V. S., Littlefair S. P., Getman F., 2011, *A&A*, **525**, A64
 Smolec R., 2016, *MNRAS*, **456**, 3475
 Unno W., Osaki Y., Ando H., Saio H., Shibahashi H., 1989, *Non-radial Oscillations of Stars*. University of Tokyo Press

Wood P. R., 1976, *MNRAS*, **174**, 531

Xiong D. R., Deng L., 2007, *MNRAS*, 378, 1270

APPENDIX A: RADIAL PULSATION MODEL GRIDS

Figures A.1 to A.16 contain the complete grids showing the numbers of unstable radial modes and the instability boundaries for each unstable mode.

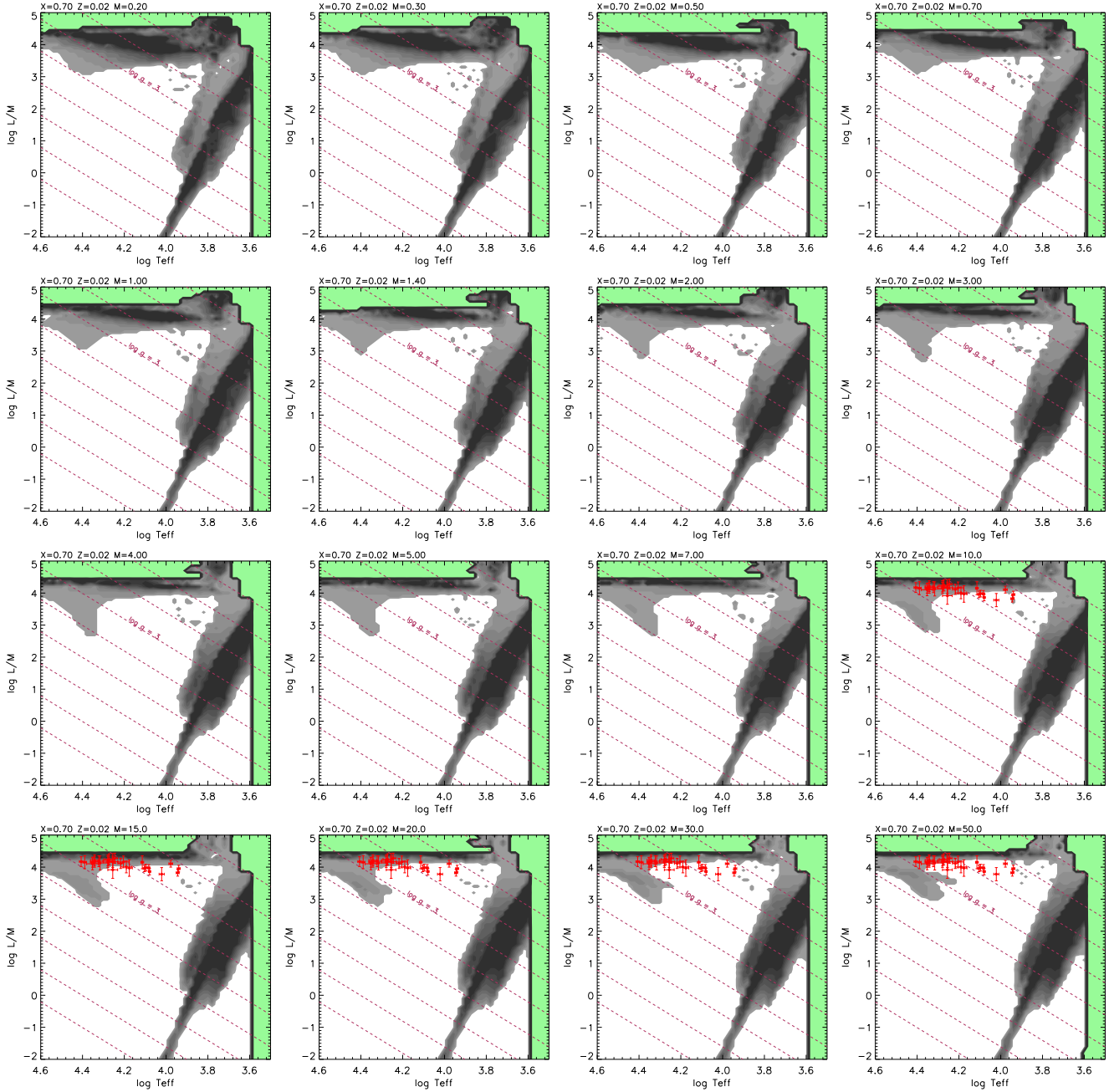


Figure A.1. Unstable pulsation modes in stars with homogeneous envelopes with hydrogen content $X = 0.70$, $Z = 0.02$, and OPAL opacities, and mass $0.20 < M/M_{\odot} < 50$, as labelled. The number of unstable radial modes is represented by grey scale contours, with the lightest shade marking the instability boundary (one unstable mode), and the darkest shade representing ten or more unstable modes. Broken (maroon online) diagonal lines represent contours of constant surface gravity at $\log g = 8, 7, 6, \dots, 1$. Models with $X = 0.7$ and $\log T_{\text{eff}} < 3.6$ were excluded. Red symbols with error bars shown on selected high-mass panels represent the observed parameters of pulsating α Cygni variables (Crowther et al. 2006; Searle et al. 2008; Furststein & Przybilla 2012).

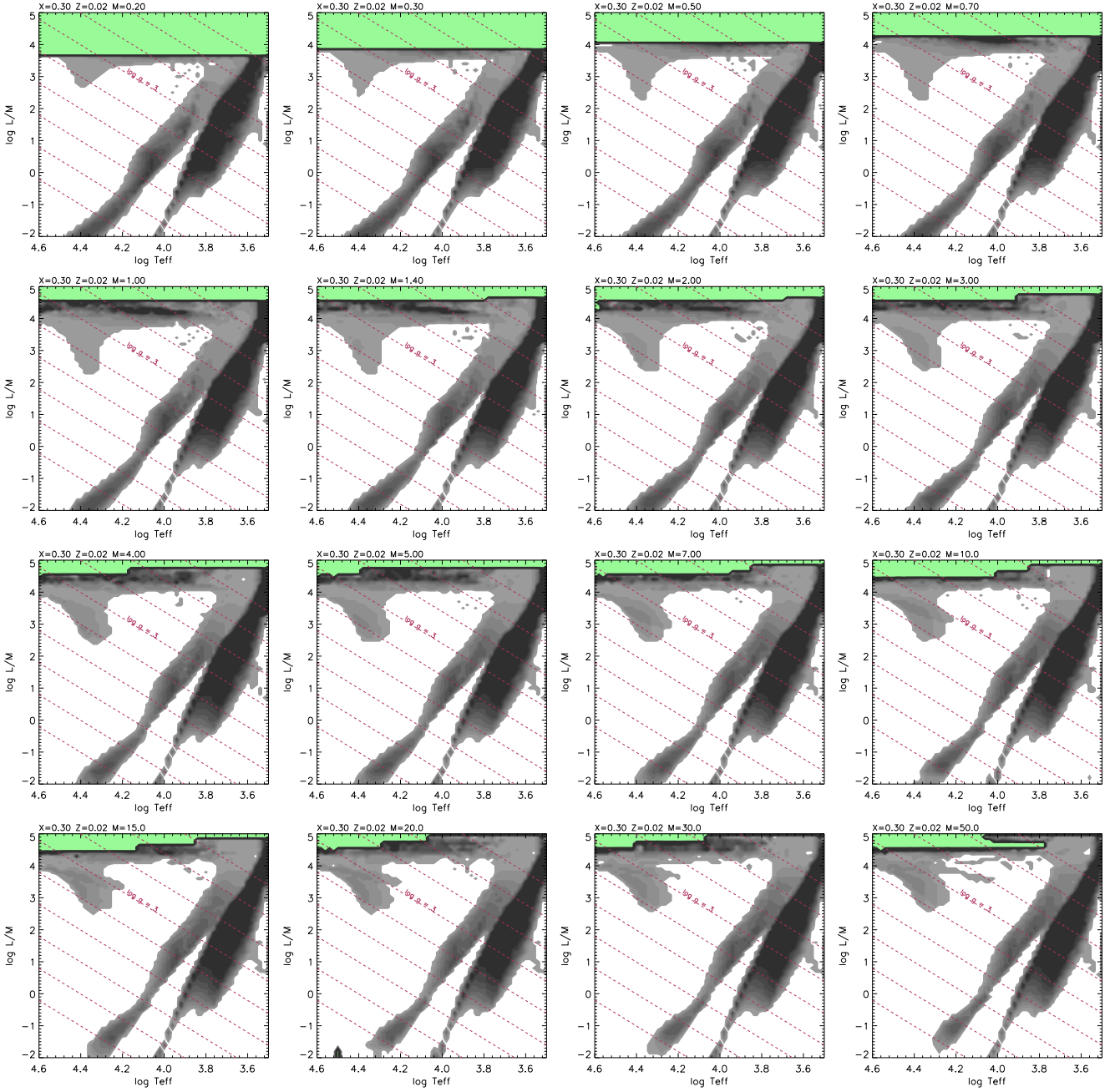


Figure A.2. As Fig. A.1 with $X = 0.30$, $Z = 0.02$.

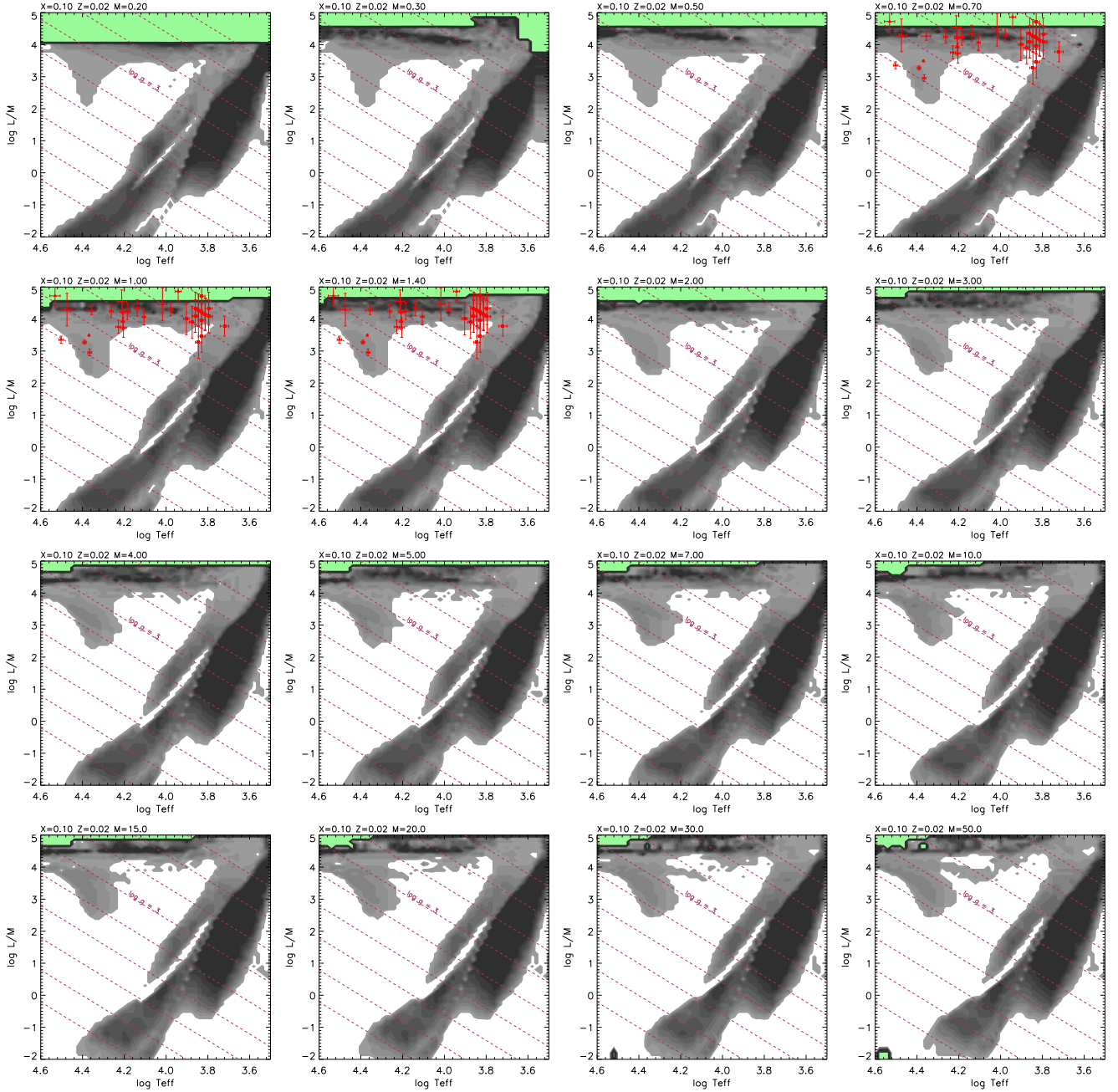


Figure A.3. As Fig. A.1 with $X = 0.10, Z = 0.02$. Red symbols with error bars shown on selected low-mass panels represent the observed parameters of pulsating low-mass hydrogen-deficient stars, including extreme helium stars and R Coronae Borealis variables (Jeffery 2008b).

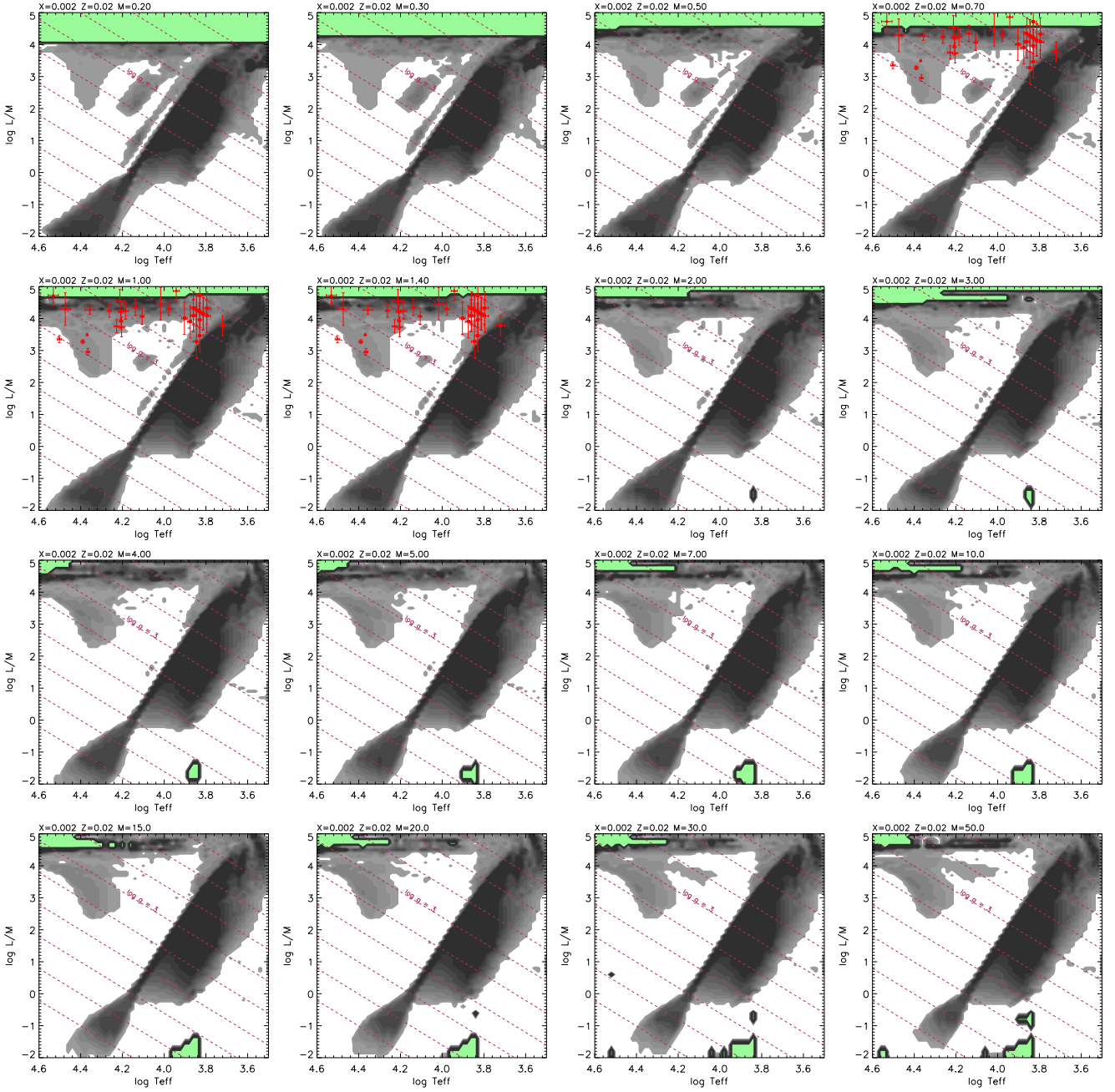


Figure A.4. As Fig. A.3 with $X = 0.002$, $Z = 0.02$.

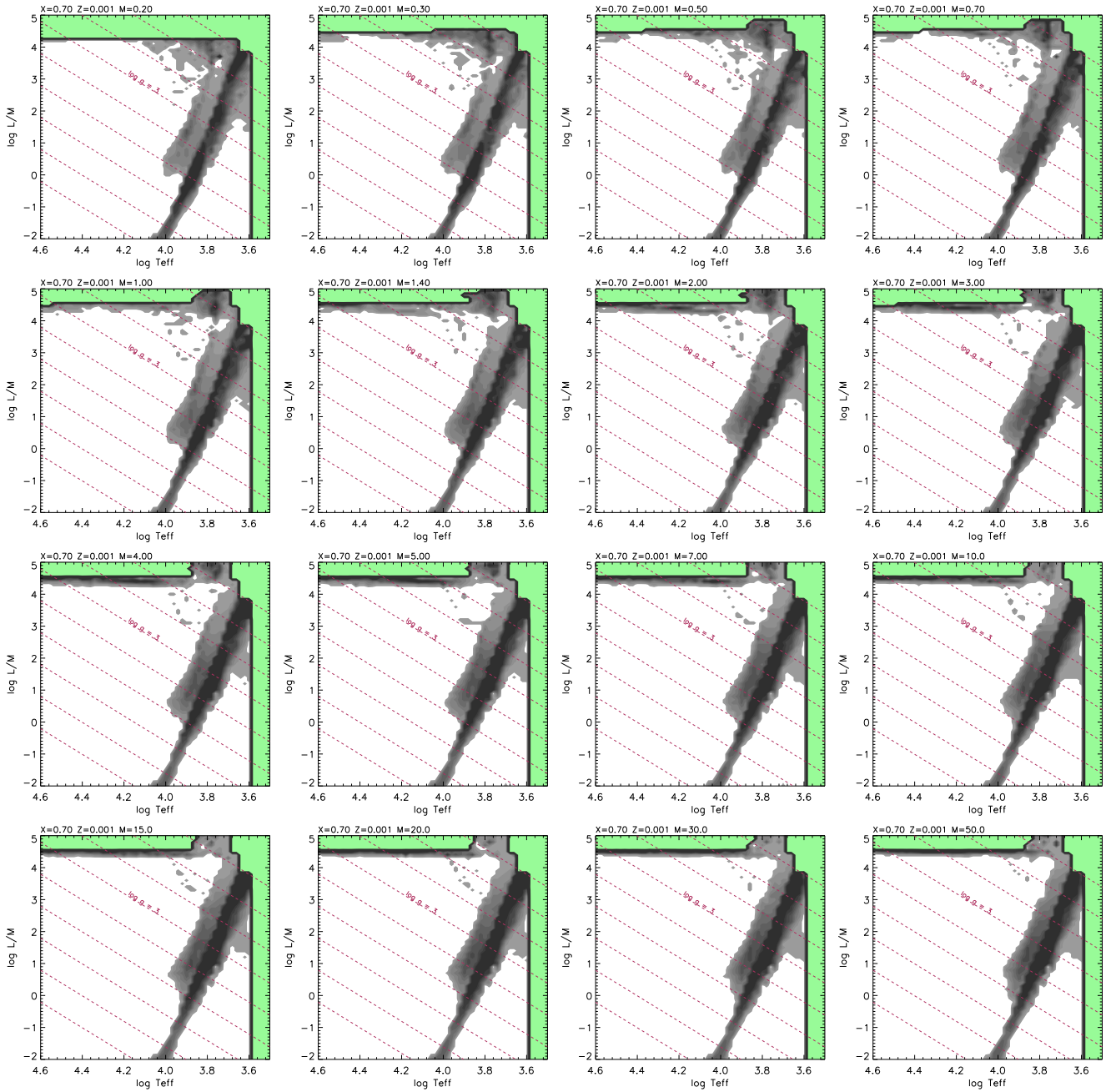


Figure A.5. As Fig. A.1 with $X = 0.70$, $Z = 0.001$.

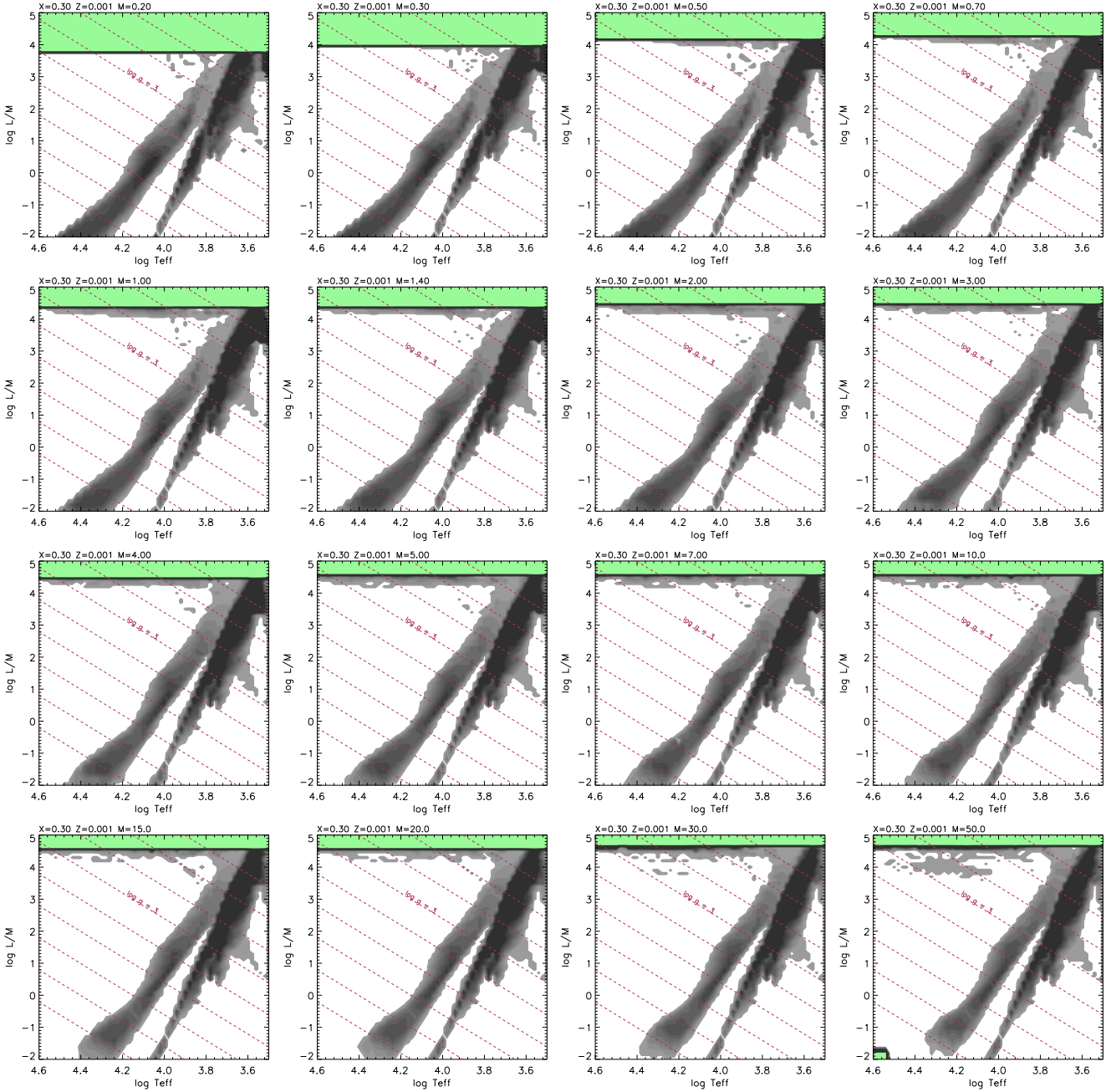


Figure A.6. As Fig. A.1 with $X = 0.30$, $Z = 0.001$.

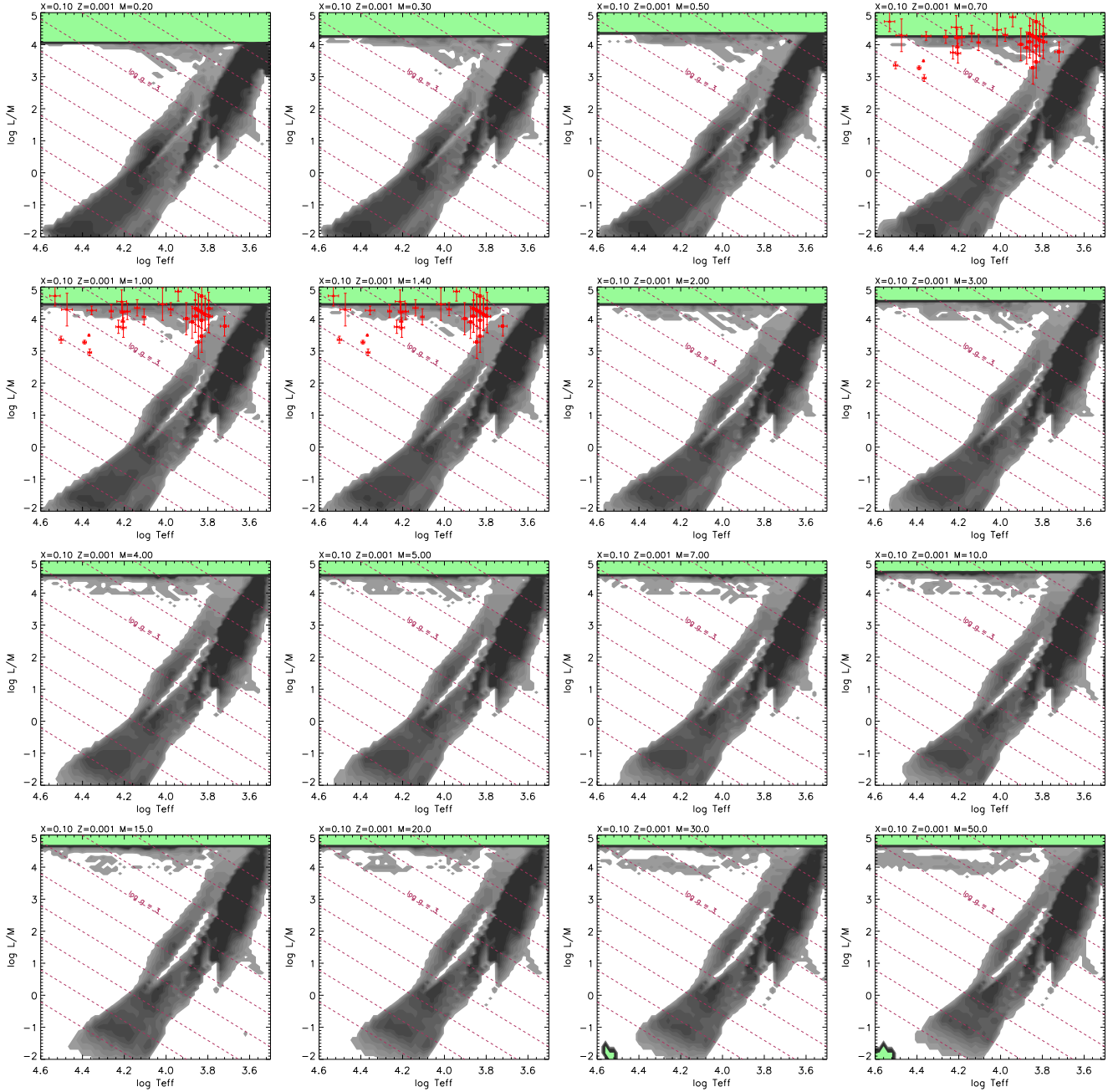


Figure A.7. As Fig. A.1 with $X = 0.10, Z = 0.001$.

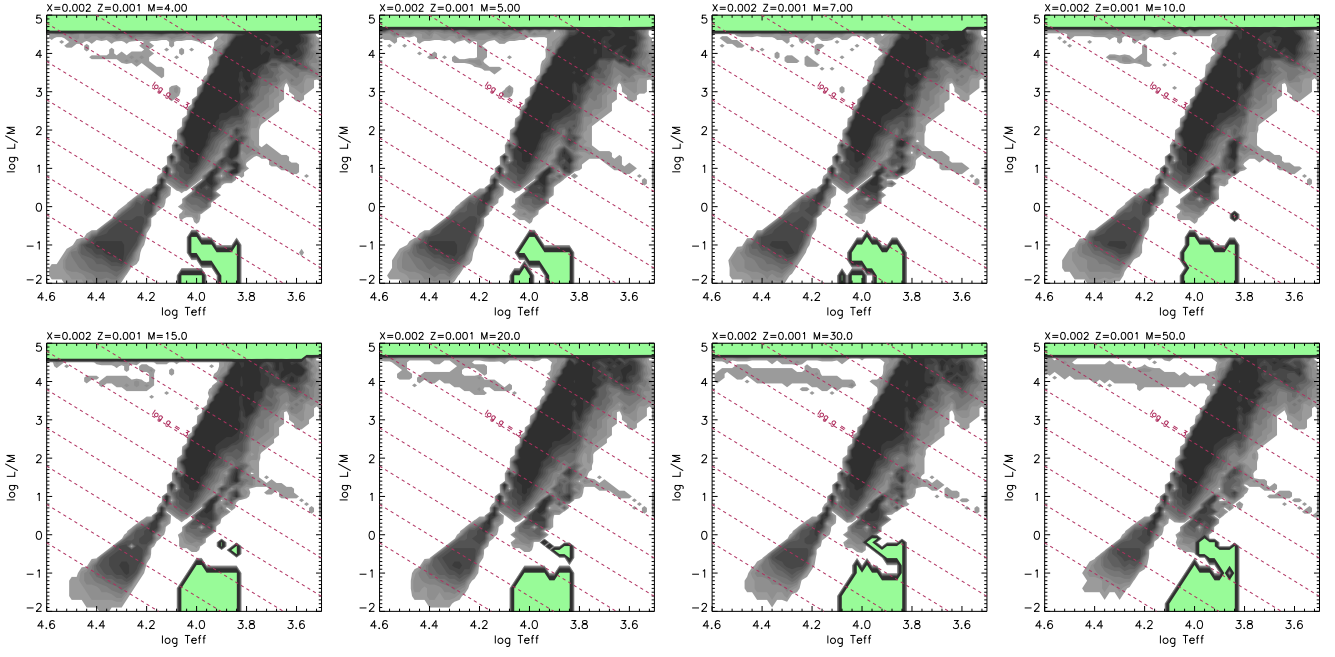


Figure A.8. As Fig. A.1 with $X = 0.002$, $Z = 0.001$, for models with $M \geq 4 M_{\odot}$. Lower-mass models encountered numerical problems at high L/M ratios.

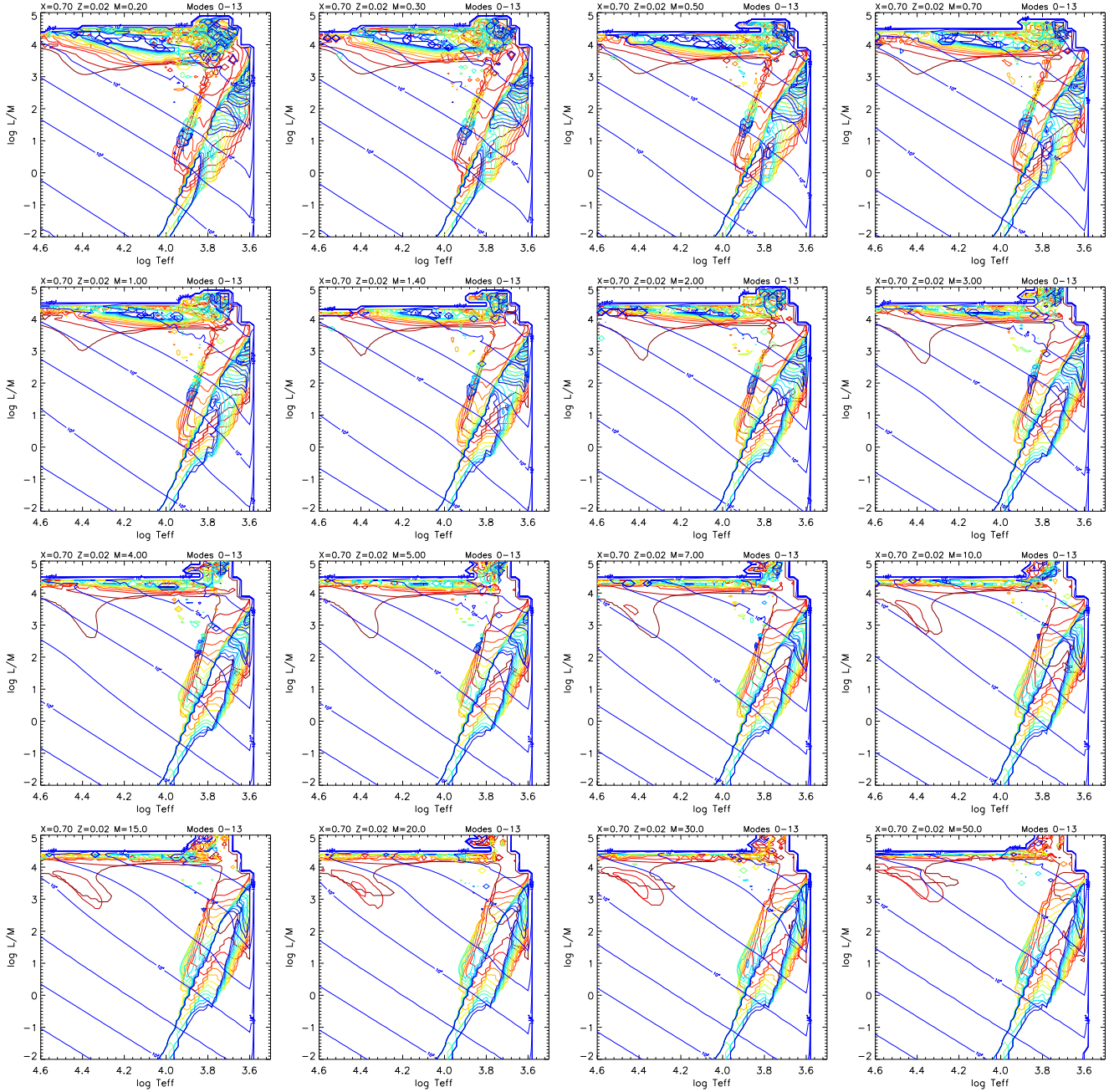


Figure A.9. Unstable pulsation mode boundaries in stars with homogeneous envelopes with hydrogen content $X = 0.70$, $Z = 0.02$, and OPAL opacities, and mass $0.20 < M/M_{\odot} < 50$, as labelled. The boundaries of unstable radial modes are represented by coloured contours, with the darkest red representing the boundary of the fundamental ($n = 0$) mode, with increasing higher orders represented progressively by colours of increasing frequency (orange, yellow, green, blue ...). Models with $X = 0.7$ and $\log T_{\text{eff}} < 3.6$ were excluded. Solid blue lines represent contours of equal fundamental radial-mode period in seconds spaced at decadal intervals.

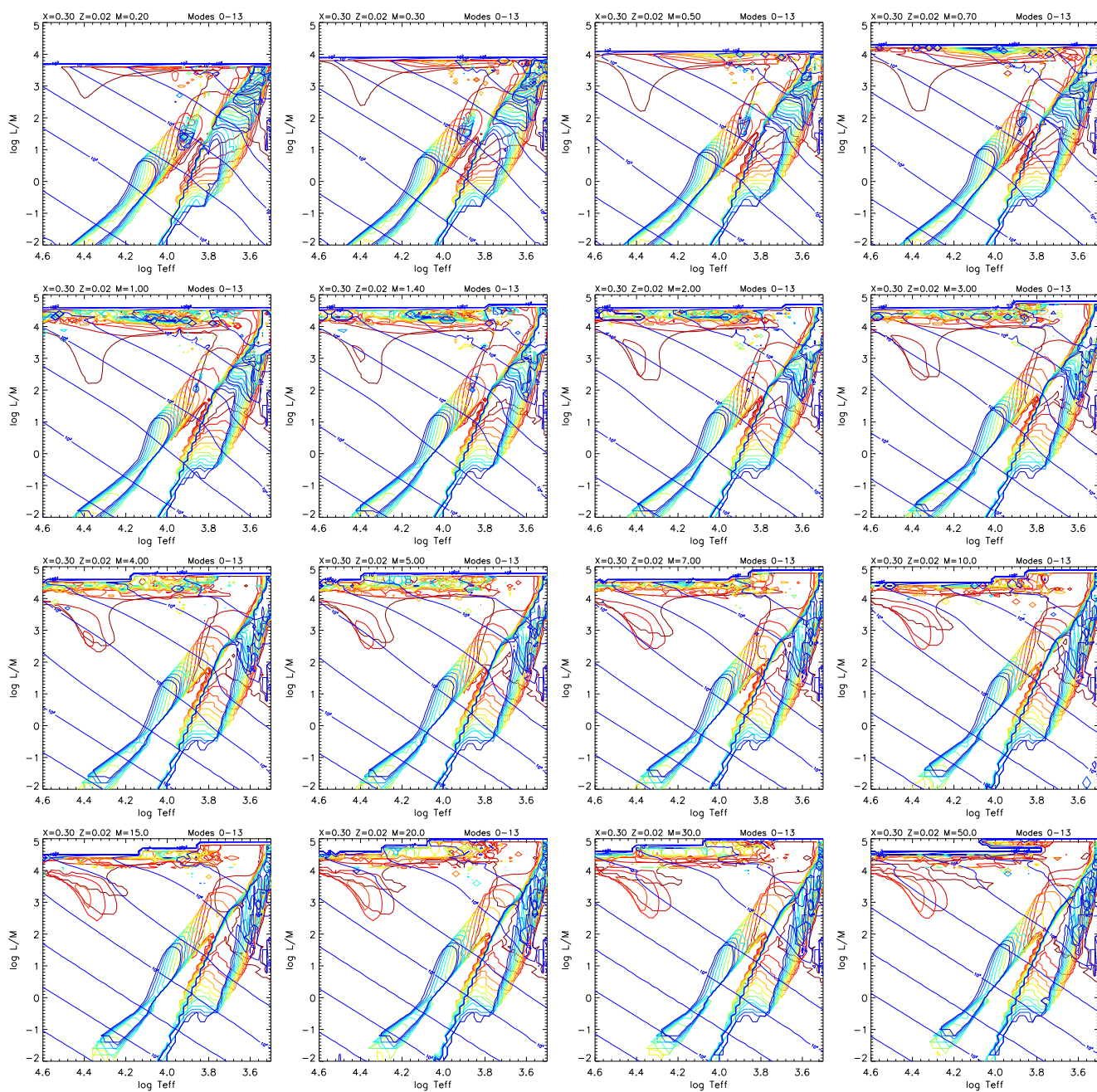


Figure A.10. As Fig. A.9 with $X = 0.30$, $Z = 0.02$.

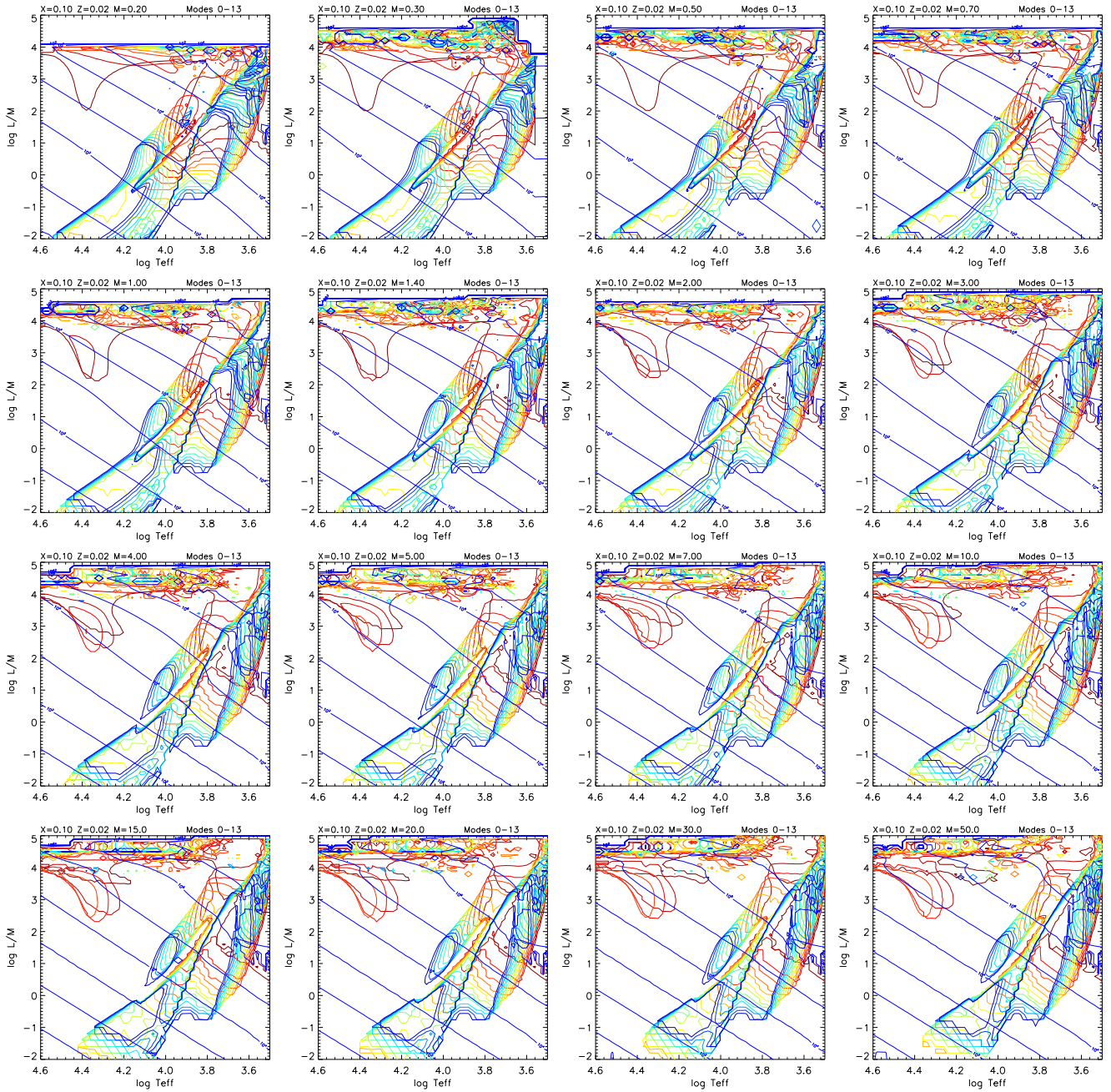


Figure A.11. As Fig. A.9 with $X = 0.10$, $Z = 0.02$.

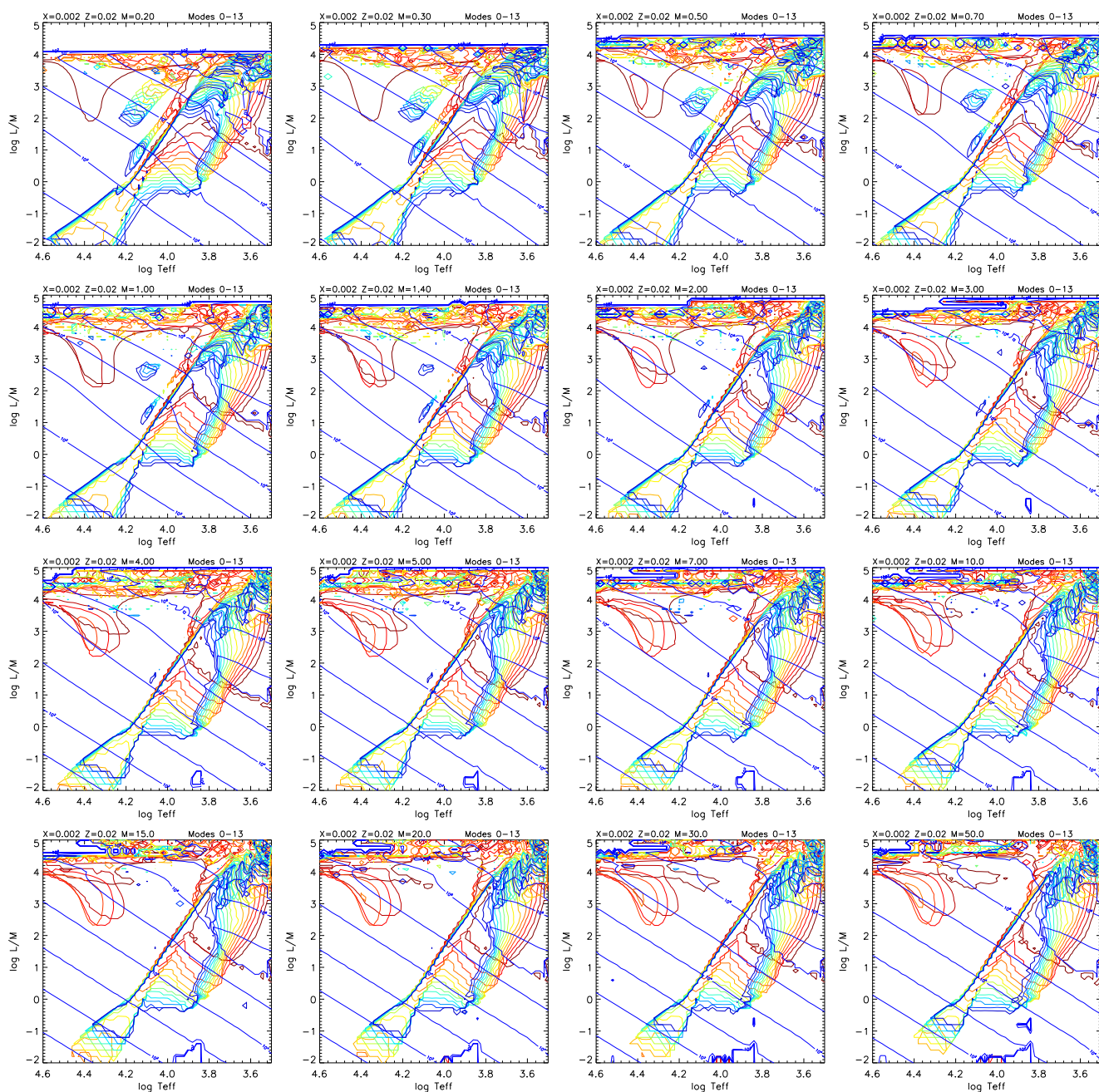


Figure A.12. As Fig. A.9 with $X = 0.002$, $Z = 0.02$.

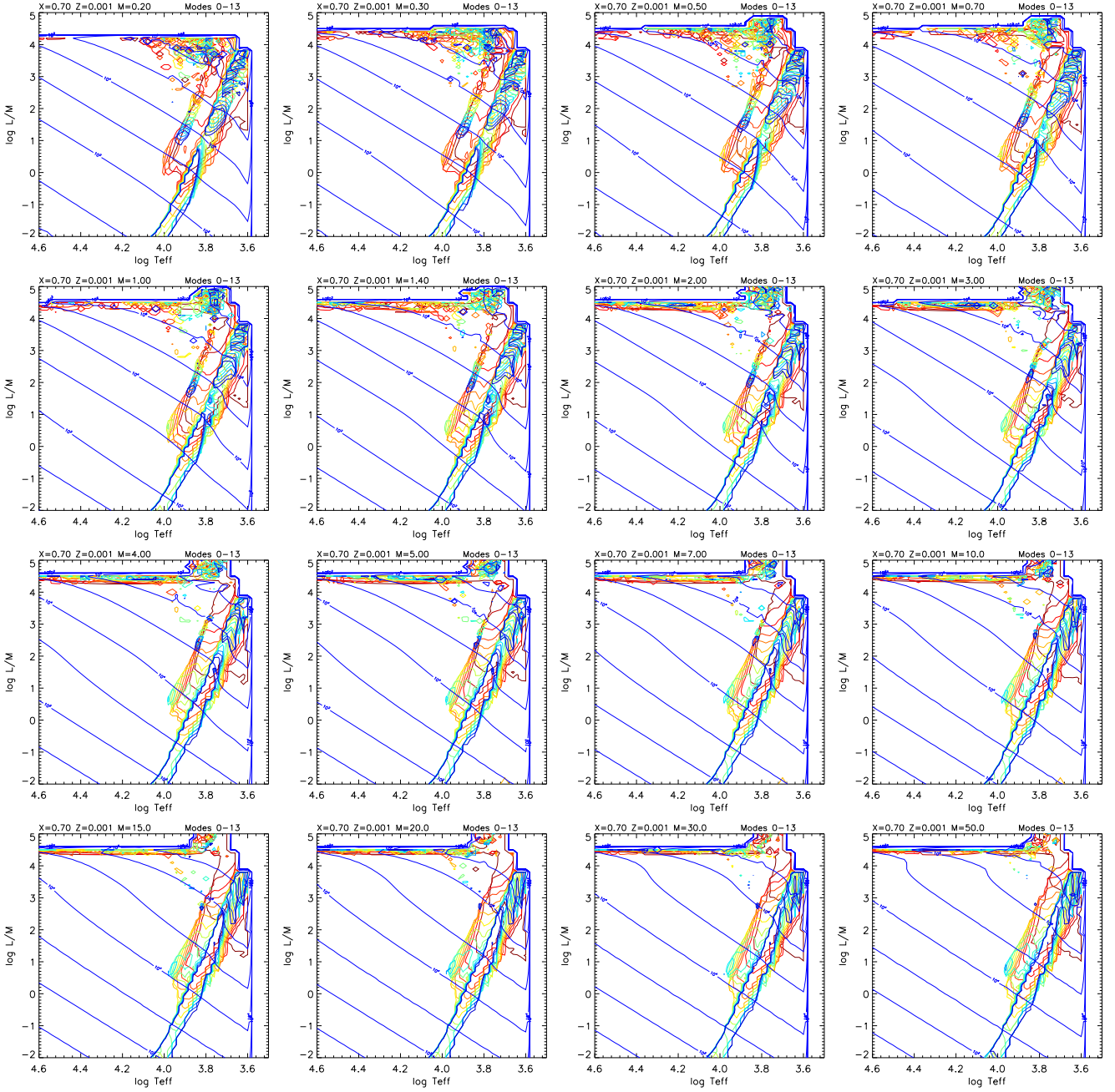


Figure A.13. As Fig. A.9 with $X = 0.70$, $Z = 0.001$.

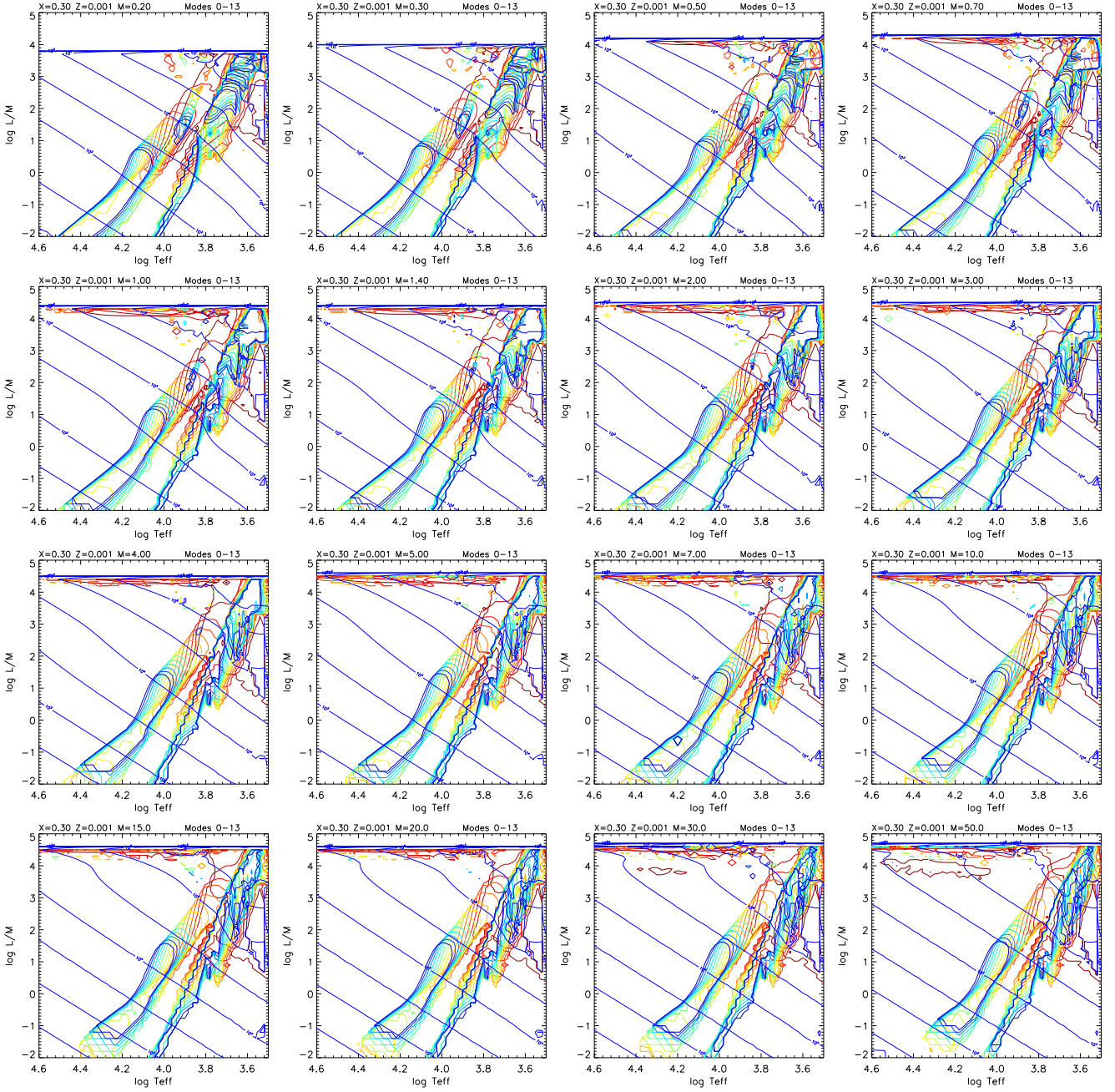


Figure A.14. As Fig. A.9 with $X = 0.30$, $Z = 0.001$.

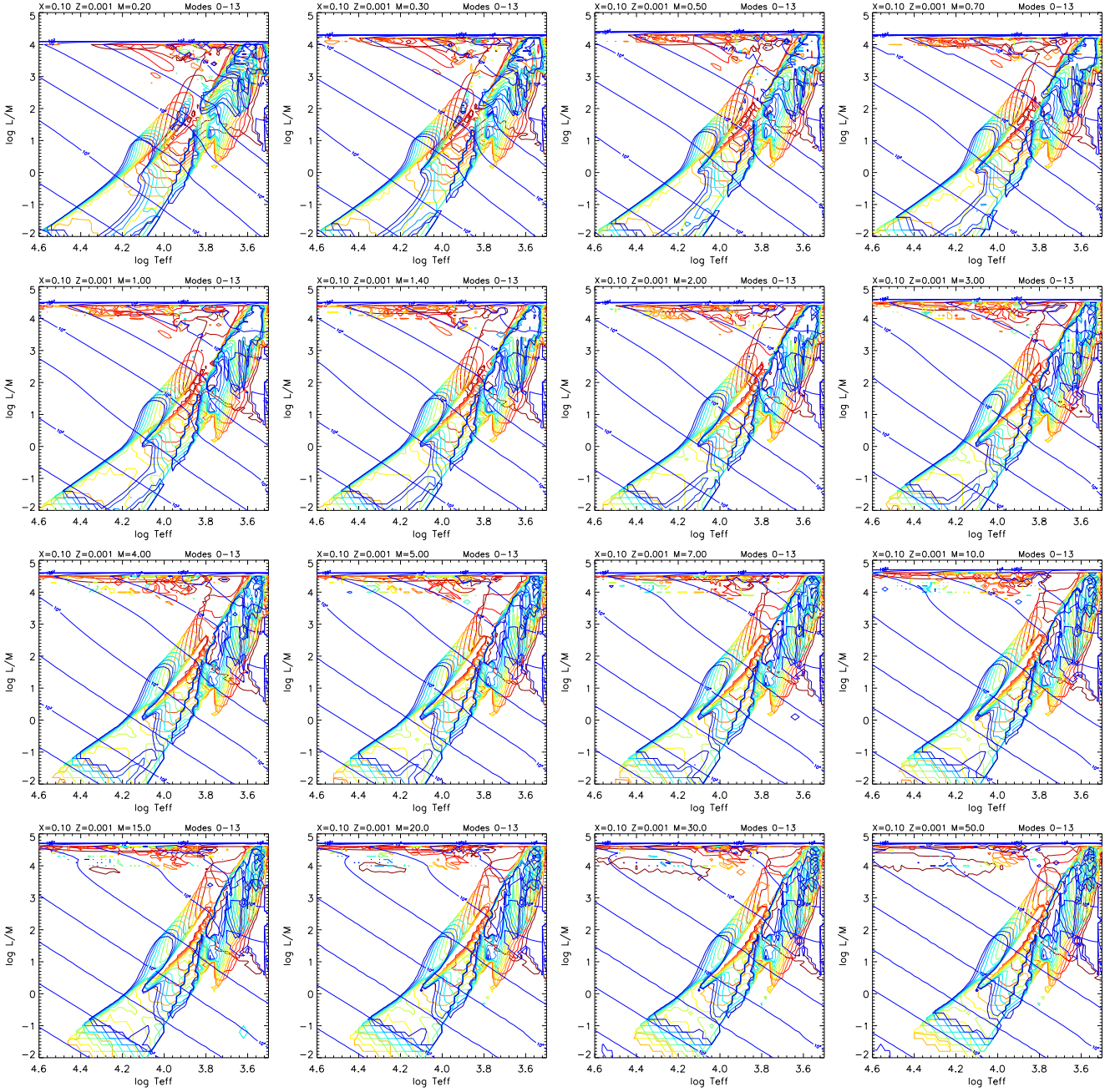


Figure A.15. As Fig. A.9 with $X = 0.10$, $Z = 0.001$.

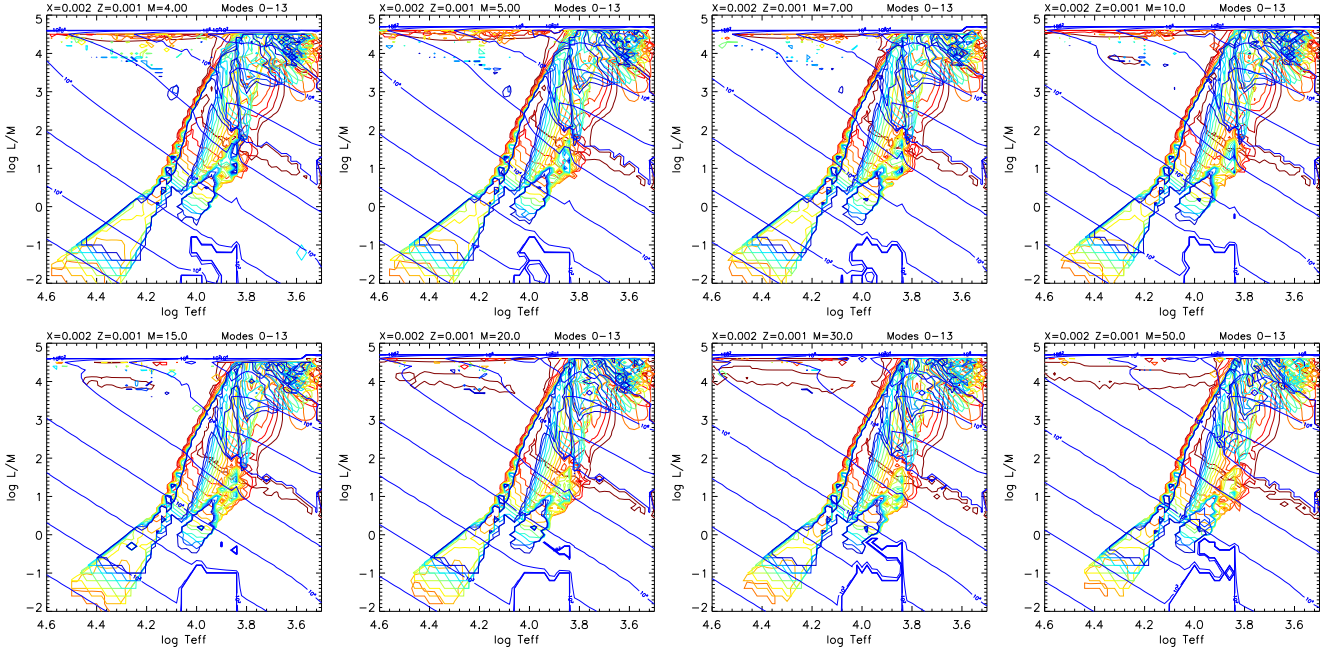


Figure A.16. As Fig. A.9 with $X = 0.002, Z = 0.001$, for models with $M \geq 4 M_{\odot}$. Lower-mass models encountered numerical problems at high L/M ratios.